Data Paper

The Rosario dataset: Multisensor data for localization and mapping in agricultural environments

Taihú Pire[1] , **Martín Mujica**[1], **Javier Civera**[2] and **Ernesto Kofman**[1]

Abstract

In this paper we present the Rosario dataset, a collection of sensor data for autonomous mobile robotics in agricultural scenes. The dataset is motivated by the lack of realistic sensor readings gathered by a mobile robot in such environments. It consists of six sequences recorded in soybean fields showing real and challenging cases: highly repetitive scenes, reflection, and burned images caused by direct sunlight and rough terrain among others. The dataset was conceived in order to provide a benchmark and contribute to the agricultural simultaneous localization and mapping (SLAM)/odometry and sensor fusion research. It contains synchronized readings of several sensors: wheel odometry, inertial measurement unit (IMU), stereo camera, and a Global Positioning System real-time kinematics (GPS-RTK) system. The dataset is publicly available from http://www.cifasis-conicet.gov.ar/robot/.

Keywords
Precision agriculture, SLAM, agricultural robotics

1. Introduction

Agriculture is one of the oldest and one of the most relevant industries for the human race. Its automation, with the goals of increasing productivity and releasing people from the most arduous tasks, has been a traditional line of research in the robotics community.

The complete automation of agriculture, however, faces several challenges of great diversity. Among others, we can cite robot localization and environment mapping, weed/crop/fruit recognition, grasping and manipulation, or navigation. The challenges might be different for each specific case, e.g., navigation will be easier in a crop field than through fruit trees. On the other hand, agricultural environments could be partially adapted to the robotic requirements if required. In this regard, it might bear a resemblance to warehouse automation, and differs from service robots and automated cars that face the additional challenge of adapting to human spaces.

Public datasets are an essential tool for the progress of a field. Sturm et al. (2012) and Geiger et al. (2013) are two relevant examples related to visual simultaneous localization and mapping (SLAM) and odometry. In this work, our aim is to contribute with the release of a public dataset for the tasks of localization and mapping in agricultural environments. The number of public datasets in the field of agricultural robotics, although increasing, is still insufficient.

Visual localization and mapping in agricultural environments presents a set of specific challenges, which is the motivation for recording this dataset. The most relevant challenges are insufficient or repetitive texture (particularly challenging for loop closing), small deviations from the rigid world assumption due to the wind, poor geometry (in many cases, just the flat ground plane), irregular terrain (with the associated jumpy motion), and a high variety of lighting conditions due to clouds passing overhead or direct sunlight. We believe that our dataset is a significant contribution to benchmark existing algorithms for agricultural applications and develop new ones that are more suited to the particularities of agricultural scenes.

We organize the rest of the paper as follows. In Section 2, we present the most recent and relevant work related to datasets for agricultural robotics. In Section 3, we present the robot used to record the dataset along with its sensors

[1]CIFASIS, French Argentine International Center for Information and Systems Sciences (CONICET-UNR), Argentina
[2]I3A, University of Zaragoza, Spain

Corresponding author:
Taihú Pire, CIFASIS, French Argentine International Center for Information and Systems Sciences (CONICET-UNR), 27 de Febrero 210 bis, S2000EZP Rosario, Argentina.
Email: pire@cifasis-conicet.gov.ar

and hardware configuration. In Section 4, we describe the sensors calibration and the recording data methodology. Section 5 presents some experimental results that illustrate the challenges and particularities of this dataset. In Section 6 we briefly describe some scripts used to record the dataset and to post-process the recorded data. In Section 7, we summarize the conclusion and the future work.

2. Related work

The recent work by Chebrolu et al. (2017) is the public dataset most related to ours. It was recorded over 3 months on a sugar beet farm, and aims to advance research on crop/weed classification, localization, and mapping.

In the case of our dataset, we do not address long-term scene dynamics, and each recorded sequence corresponds to a different scene. As our aim is to evaluate localization and mapping capabilities, our data contains a wider array of scenes, with the aim of capturing a wider extent of challenging situations.

In the rest of this section, we give an overview of several other related datasets. The survey is limited to the most recent and relevant works, with focus on visual data, and organized into two groups: first, those works focusing in localization and mapping and, second, those targeting agricultural applications.

2.1. Datasets for localization and mapping

There exist many localization and mapping datasets. If we classify them by scene type, some of the most relevant are as follows.

- *Indoor scenes.* Ruiz-Sarmiento et al. (2017) used ground robots and with semantic annotations. Burri et al. (2016) recorded data from quadrotors and with geometric ground truth for the trajectory and the scene. Sturm et al. (2012) presents a classic dataset recorded with a RGB-D camera.
- *Outdoor urban scenes.* Some are taken by sensorized cars (Blanco-Claraco et al., 2014; Pandey et al., 2011), others by small mobile robots (Carlevaris-Bianco et al., 2016; Smith et al., 2009), and others by quadrotors (Majdik et al., 2017). Maddern et al. (2017) focused on life-long mapping from car vehicles.
- *Outdoor rural scenes.* Miller et al. (2018) released visual–inertial sequences taken from a canoe navigating along a river. The dataset of Griffith et al. (2017) is composed of several surveys over several years of a lake from an autonomous surface vehicle. Leung et al. (2017) presented data from an underground mine.
- *Simulated planetary scenes.* From all the existing datasets, we can name, for example, Furgale et al. (2012b) and Tong et al. (2013)

2.2. Datasets for agricultural applications

There are fewer datasets that are specifically related to agricultural robotics than those devoted to odometry and SLAM. However, recently, there has been an emergence of several relevant datasets owing to the growing importance of this application. In the next paragraph we mention several recent datasets that have very different aims, reflecting the wide array of challenges in agricultural robotics.

Haug and Ostermann (2014) presented a dataset containing real images for weed/crop classification. Owing to the difficulty of scaling the dataset size with manual annotation, Di Cicco et al. (2017) addressed the same problem creating a synthetic dataset. Sa et al. (2018) addressed weed/crop classification from multispectral images recorded by a micro aerial vehicle (MAV), using a deep neural network and releasing the data used. Pezzementi et al. (2018) targeted person detection in off-road and agricultural scenes. The dataset presented by Fentanes et al. (2018) contains soil compaction data, with the aim of advancing autonomous soil compaction mapping by robots. Dias et al. (2018) addressed the automated perception of bloom intensity (the number of flowers in an orchard), which should guide operations such as pruning and thinning for the desired fruit features. It releases an annotated dataset with pixelwise flower labels in high-resolution images. Alencastre-Miranda et al. (2018) collected a dataset for classifying the damage that automated harvesting caused in sugarcane billets.

3. The weed-removing robot

In this section, we describe the robot that we used to record the dataset, along with its sensors.

3.1. The robot

The robot consists of a mobile platform with four wheels (see Figure 1). It has been designed to work autonomously in large areas; and hence its power source is four batteries that are charged by photovoltaic cells in the top of the vehicle.

The robot has been designed to automate the weed-removing tasks in large crop fields. Our aim is that the weeds and the crops are classified using visual data, and a tool (currently being developed) removes the weed without damaging the crops. The robot should navigate through the field autonomously and should keep track of the state of each land piece; hence, it needs accurate localization and mapping capabilities in this environment.

The robot motion is controlled by four brushless motors (one per wheel) and their drivers. For the front wheels direction, a stepper motor has been built with the appropriate reduction and encoder.
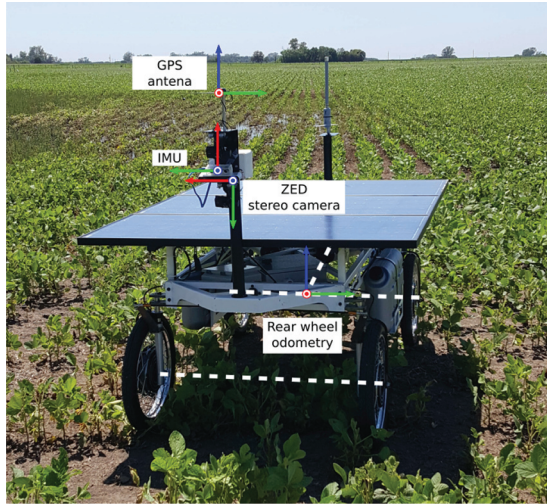
Fig. 1. The weed-removing robot and its sensors. The right camera coordinate frame is not shown for clarity.

3.2. The sensors

Figure 1 shows the sensors that are mounted in the robot and their respective local frames. The main technical details of the sensors are as follows.

- **Stereo Camera.** We used the *ZED stereo camera*.[1] The camera baseline is 12 cm. We recorded synchronized left and right images at a resolution of 672×376 px, and at a frame rate of 15 Hz.
- **Motors encoders.** We used three Hall effect sensors coupled with each wheel to measure rotational angle increments. From this data, using a kinematic model of our robot, we extracted its linear and angular motion.
- **Global Positioning System real-time kinematics (GPS-RTK).** We used two *GPS-RTK Reach*[2] modules, one mounted on the robot and another one on the base station. The GPS-RTK frequency is 5 Hz. Its accuracy was characterized in our previous work (Pistarelli et al., 2017). The base station consists of a Reach module connected to a Tallysman TW4721 antenna with IP67 protection. It is mounted on a 322×247 mm ground plane that far exceeds the 100×100 mm suggested by the manufacturer of the GPS-RTK, giving it superior rejection of bouncing signals from nearby structures (*multipath signals*). The connection between the two GPS-RTK modules was made through a WiFi network using two routers. The first, a MikroTik Metal G-52SHPacn, was placed in a fixed base station, whereas the second, a MikroTik Groove GA-52HPacn, was placed on the robot. The routers were chosen due to their high transmission power and receiver sensitivity. The main difference between them is that the one placed on the robot has a lower power consumption. To energize both systems, a module powered by four rechargeable lithium cells with a total capacity of 10.400 mAh was chosen to integrate the *switching*

regulated charge and output system of 5 V voltage in the same container.

- **Inertial measurement unit (IMU).** The IMU that we used is the LSM6DS0, that is built in the *TARA stereo-inertial sensor*.[3] The IMU rate was set to 140 Hz.

Although our sensor equipment included the TARA stereo camera, its auto-exposure setting was not appropriate for our outdoor scenes and produced burned images. We then had to discard the images, but we kept the IMU data.

The ZED stereo camera, IMU, and motors encoders were connected by USB 3.0 to the robot's computer. The GPS-RTK information was read through a WiFi network.

3.3. The computer

All the sensor data we recorded was timestamped and stored in an onboard robot computer. We used a MINI-PC Intel® NUC Kit[4] (Intel Celeron J3455 CPU, quad-core 2.3 GHz, and 8GB DDR3 RAM) with Ubuntu 16.04. The supplied voltage (12 V) came from the robot batteries. In order to record data as soon as it arrives to the Operative System and avoid disk-writing delays, we used a solid state disk (SSD; specifically, a 240GB Western Digital SSD WDS 240G1G0A) as the storage unit.

4. The dataset

In this section, we detail the calibration of the robot sensors and the format of the recorded data.

4.1. Calibration

The extrinsic and the intrinsic calibrations of all sensors (for each sequence) are stored in the files `calibration.txt` (Table 1 lists the extrinsic parameters). The calibration file includes the camera and IMU intrinsic parameters, and the transformations between all the sensors.

4.1.1. Intrinsic parameters. For each camera of the ZED stereo we used a standard pinhole model with radial–tangential distortion. We calibrated the intrinsics of each camera with Kalibr (Maye et al., 2013).

We used the *Allan variance* method (Allan, 1966) for estimating the IMU noise model. The noise model is given by accelerometer noise density (σ_g), accelerometer random walk bias (σ_{bg}), gyroscope noise density (σ_a), gyroscope random walk bias (σ_{ba}), and the sampling rate $\left(\frac{1}{\Delta t}\right)$. The specific values for the IMU noise model are listed in Table 1.

4.1.2. Extrinsic parameters. We chose the local frame of the rear_wheel_odometry as our robot base_link, and referenced the extrinsics of all the other sensors to such frame. We used Kalibr (Furgale et al., 2012a, 2013) to calibrate the stereo extrinsics (the relative pose between the left and right cameras) and the relative transformation between the cameras and the IMU.

Table 1. Rigid transformations between the different coordinate frames involved in the system. The translation is given by *x*, *y*, and *z*, and the rotation by the quaternion *q*. The transformations are defined to convert points from the Child Frame ID to the Frame ID. The rigid transformation between the base_link and the imu coordinate frames changes for each sequence and therefore is not listed here.

Frame ID	Child Frame ID	x (m)	y (m)	z (m)	q_x	q_y	q_z	q_w
rear_wheel_odometry	base_link	0	0	0	0	0	0	1
base_link	gps	1.8	−0.030	1.593	—	—	—	—
imu	left_camera	−0.031	−0.077	0.026	0.058	0.019	0.703	0.708
imu	right_camera	−0.030	0.042	0.033	0.064	0.012	0.703	0.708

Table 2. IMU calibration parameters.

Parameter	Value	Units
$\frac{1}{\Delta t}$	142.0	Hz
σ_g	8.2739	$\frac{\text{rad}}{\text{s}} \frac{1}{\sqrt{\text{Hz}}}$
σ_{bg}	8.7367	$\frac{\text{m}}{\text{s}^2} \frac{1}{\sqrt{\text{Hz}}}$
σ_a	0.0017	$\frac{\text{rad}}{\text{s}^2} \frac{1}{\sqrt{\text{Hz}}}$
σ_{ba}	0.0057	$\frac{\text{m}}{\text{s}^3} \frac{1}{\sqrt{\text{Hz}}}$

We calibrated the rigid transformation between the odometry coordinate frame (rear_wheel_odometry) and the left camera frame (left_camera) as follows. First, we estimated the motion of the robot referred to the left camera frame in small straight segments of our data. We used the stereo SLAM system S-PTAM (Pire et al., 2017) for this. Then, we averaged the normalized estimated positions to estimate the local motion vector. We calculated the rotation matrix between such motion vector and the forward axis of the camera $[0, 0, 1]$. We denote this rotation as $\mathbf{R}(\theta)$, where θ is the angle between the motion and the camera z-axis. The $\mathbf{R}(\theta)$ rotation, composed with the 90° rotations required to align the axis of both frames, forms the rotation between the odometry and the left camera coordinate frames, as detailed in the following equation:

$$\mathbf{R}^{\text{rc}} = \mathbf{R}_z(90°)\mathbf{R}_x(90°)\mathbf{R}(\theta) \qquad (1)$$

where $\mathbf{R}^{\text{rc}}$ denotes the rotation matrix between the left camera frame and the odometry frame. The rotation matrices $\mathbf{R}_z(90°)$ and $\mathbf{R}_x(90°)$ are the 90° rotations around the z- and x-axis, respectively. We estimated the translation part of the rigid transformation between both sensors by directly measuring them on the robot.

To keep the left and right camera as child frames of the IMU frame, we used the transformation between the odometry frame and the left camera frame ($\mathbf{T}^{\text{rc}}$), along with the transformation between the left camera and the IMU ($\mathbf{T}^{\text{ci}}$) to calculate the relative pose between the odometry frame and the IMU frame $\mathbf{T}^{\text{ri}}$, which is the one used in the transformations tree:

$$\mathbf{T}^{\text{ri}} = \mathbf{T}^{\text{rc}}\mathbf{T}^{\text{ci}} \qquad (2)$$

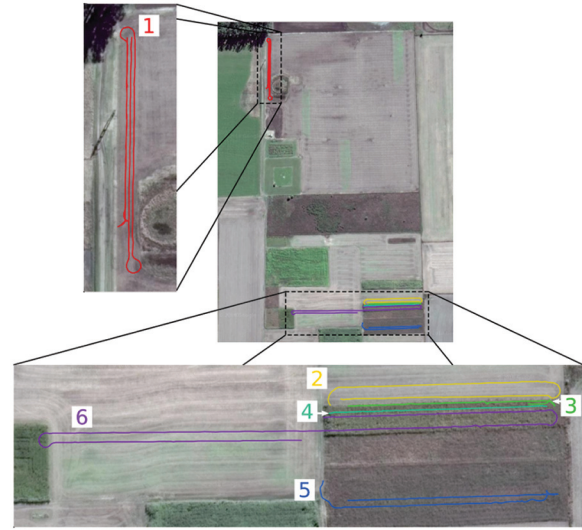The relative transformation between the rest of the sensors (GPS-RTK and odometry) was calibrated using

Fig. 2. GPS-RTK trajectories for the six sequences of the dataset.

AprilTags (Olson, 2011). We attached the tags to the sensors and estimated their relative transformations from multiple views taken by an external camera. In particular, we used the ar_track_alvar[5] ROS package.

4.2. Data synchronization

As we are working with end-user sensors (ZED stereo camera, TARA visual–inertial sensor, and GPS-RTK Reach modules), all data was synchronized by software at the level of user applications in the Operative System. The data was straightforwardly recorded on an SSD in the robot on-board computer. We used a precision of milliseconds for measurement timestamp labels.

4.3. Data collection and summary

The data was collected on two separate days in the agricultural fields used by the Faculty of Agricultural Science at the National University of Rosario, Argentina. We recorded six sequences, with a total trajectory length around 2.3 km and a total time around 30 min.

Figure 2 shows the GPS-RTK trajectories of the six experiments. We commanded the robot to navigate along the furrows, with 180° turns at their ends. Such trajectories

Table 3. Sequences description.

Sequence	Difficulty	Length (m)	Duration (min)	Sequence ID (date_time)	Summary
1	Easy	615.15	9.3	2017-12-26_12:25:45	$3 \times 180°$ turn Occasional backwards motion People (occasional) Partial occlusions Easily visible furrows Green crops
2	Easy	320.16	4.4	2017-12-29_11:13:55	$1 \times 180°$ turn Dried crops People (occasional) Hardly visible furrows
3	Medium	169.45	3.3	2017-12-29_11:23:00-part1	$1 \times 180°$ turn Occasional backwards motion Dried and green crops Easily visible furrows
4	Medium	152.32	2.7	2017-12-29_11:23:00-part2	No turns Easily visible furrows Green crops
5	Difficult	330.43	5.2	2017-12-29_11:47:35	$1 \times 180°$ turn Occasional backwards motion Varied furrow visibility People (occasional)
6	Difficult	709.42	9.8	2017-12-29_12:00:07	$2 \times 180°$ turn People (occasional) Road crossing

are less damaging for the crops, so we assume robots similar to ours will follow similar trajectories in agricultural applications. Owing to the non-holonomic constraints of our platform and distance between furrows, $180°$ turns require maneuvering and short backwards motions.

Table 3 contains more technical details for each of the sequences and a qualitative grade (from easy to difficult) and summary. The grade is based on our visual inspection and the results offered by visual SLAM baselines (see Section 5). The data was recorded aiming to show a high variety of conditions in the fields: from green to dried crops, and from low to high vegetation density (that makes the furrows more or less visible). Such variations are reported in the table.

In addition to the particularities of each sequence, the data presents the challenges associated with agricultural applications mentioned in the introduction. The feature density is irregular. Visual tracking is difficult, owing to texture similarities and non-rigid motions. The latest are mainly caused by light wind, and also by people that occasionally enter the field of view of the cameras. The robot motion is bumpy owing to the uneven terrain, which makes tracking harder. The rolling shutter of the *ZED stereo camera* adds an extra complexity, but we believe that such cameras are the most reasonable option for massive robot deployment owing to their low cost.

Figure 3 shows several sample images from all the sequences of the dataset. Note the mentioned variability in the crop and field conditions, the low texture, and the repetitive patterns.

4.4. Data formats

Figure 4 shows the dataset folder structure. We included the raw data and also the processed rosbags containing standard ROS messages, in order to facilitate its use. The data is, specifically, stored as follows.

4.4.1. Raw data

- **ZED stereo camera.** There is a folder containing both left and right images in `.png` format. The image size is 672×376 and the naming convention is `<camera>_<timestamp>.png`.
- **IMU.** The file contains the measurements of the angular velocity and linear acceleration along the three axes as `<timestamp> <gyro[x,y,z]> <acc[x,y,z]>`.
- **GPS-RTK.** The data follows the National Marine Electronics Association (NMEA) standards, giving the traditional latitude–longitude information, but also ground speed and satellite status. Each NMEA sentence has its own timestamp.
- **Odometry.** We record the information from the wheel motors at a frequency of 10 Hz, along with the current timestamp. This information consists of the linear velocity of each motor and the current angle of the stepper motor that drives the direction. The measurements are contained in a file where each line is structured as `<timestamp> <vel_left> <vel_right> <angle> <direction>`.
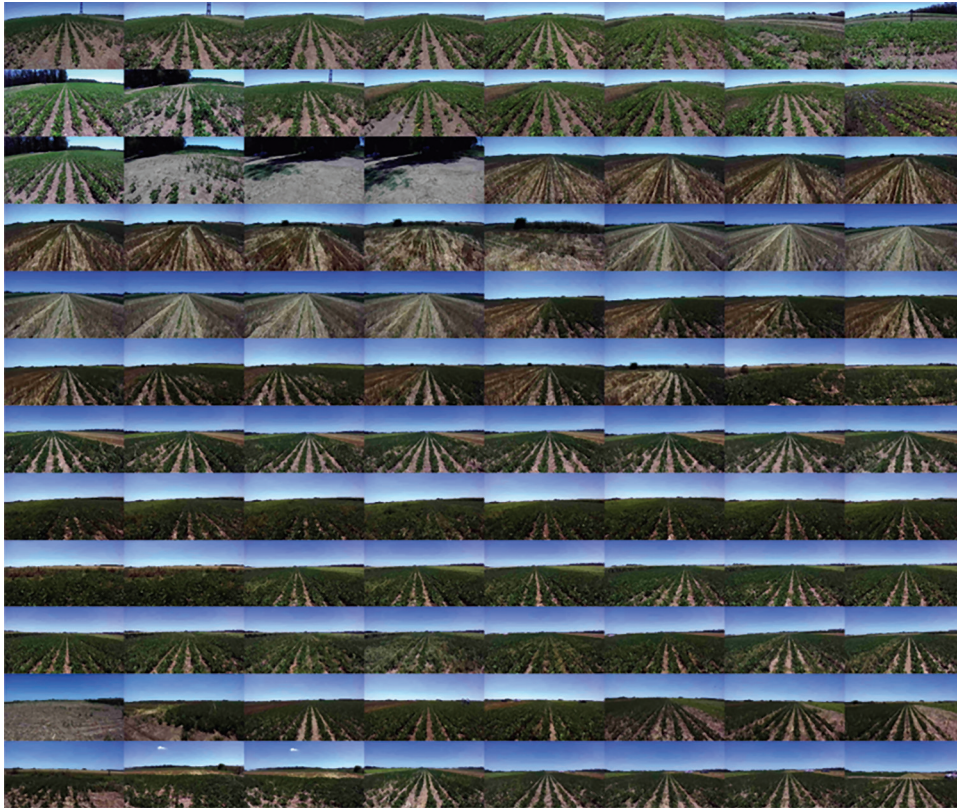
Fig. 3. Sample images of all the sequences of the dataset.
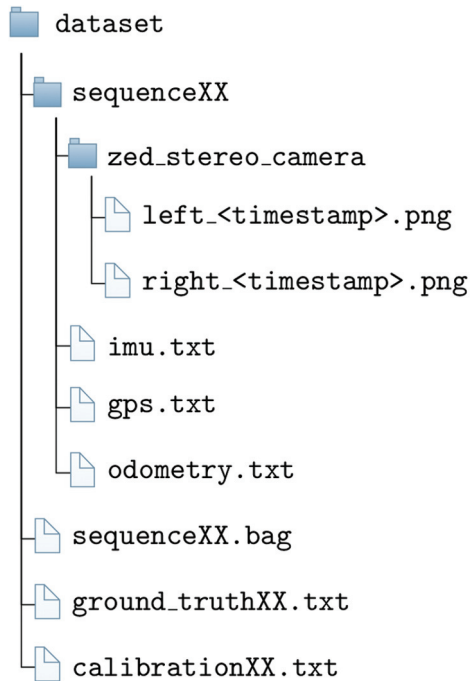

Fig. 4. Dataset structure. The suffix XX refers to the sequence numbers (01..06).

4.5. Rosbags

In addition to the raw data, we provide a rosbag for each sequence, the data being adapted to fit into ROS standard messages. This allows the use of the dataset with ROS-based software with minimum overload. The type of messages included in the .bag files are as follows.

- **sensor_msgs/Image.msg**. Left and right images from the ZED stereo camera.
- **sensor_msgs/CameraInfo.msg**. Intrinsic and extrinsic parameters of both cameras. The right camera pose is referred to the left camera coordinate system.
- **sensor_msgs/Imu.msg**. Raw IMU measurements.
- **sensor_msgs/NavSatFix.msg**. We publish the "GGA" part of the NMEA sentences provided by the GPS-RTK. The GGA sentence includes positioning and its estimated accuracy.
- **nav_msgs/Odometry.msg**. Linear and angular velocity derived from the wheel encoders and the robot kinematic model. We also publish the integrated pose, resulting from the integration of the velocities.
- **tf/tfMessage.msg**. Extrinsic transformations between coordinate systems (see Table 1). All the extrinsic transformations between sensors are expressed as a

Table 4. Absolute trajectory error (ATE, in meters; ratio ATE over trajectory length, in %), for ORB-SLAM2 and S-PTAM in the sequences of the Rosario dataset and a selection of KITTI (X denotes tracking failure).

Sequence	ORB-SLAM2	S-PTAM
Rosario 01	1.41 (0.23%)	3.85 (0.63%)
Rosario 02	2.24 (0.70%)	1.80 (0.56%)
Rosario 03	3.50 (2.06%)	2.37 (1.40%)
Rosario 04	2.21 (1.45%)	1.49 (0.98%)
Rosario 05	2.23 (0.68%)	X
Rosario 06	5.19 (0.73%)	X
KITTI 03	0.60 (0.11%)	1.66 (0.30%)
KITTI 05	0.80 (0.04%)	2.85 (0.13%)
KITTI 06	0.80 (0.06%)	2.99 (0.24%)

Fig. 6. Feature tracks example: yellow, reprojection of map points tracked in this frame; red, point correspondences; blue, map points that cannot be tracked. Note the high number of these latter points.

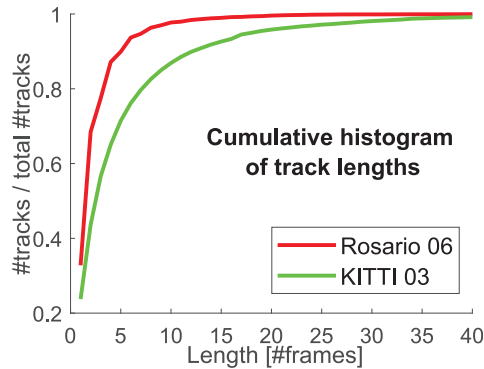**Fig. 5.** Cumulative histogram of the length of S-PTAM feature tracks, for a representative sequence of the Rosario and KITTI datasets.

As having the ground-truth data in the robot frame (base_link) is necessary for comparing the trajectories, we computed the rotation between the robot trajectory and the GPS-RTK positions in small data subsets (less than 10 m) of each sequence, where the robot is approximately moving in a straight line. We obtained the trajectory performed by the robot using the visual SLAM system S-PTAM (Pire et al., 2017, 2015), which provides a highly accurate pose in highly textured environments. Observe that S-PTAM has been run offline in order to guarantee the best performance.

The rotation transformation between both trajectories is computed using the Horn method provided by Sturm et al. (2012) and applied to the original GPS data to obtain the ground truth presented in the dataset.

5. Baselines

We run two state-of-the-art baselines for stereo SLAM, ORB-SLAM2 (Mur-Artal and Tardós, 2017) and S-PTAM (Pire et al., 2017), in order to illustrate the characteristics and challenges of our dataset. Both systems were run with their default configuration. Table 4 lists the absolute trajectory error (ATE, as defined by Sturm et al. (2012)) and, in parentheses, the ratio of such error over the trajectory length. For comparison, we also show the same metrics for both system in three sequences of KITTI dataset (Geiger et al., 2013), comparable in length to our own.

Note how the error ratios for the Rosario dataset are significantly higher than those using the KITTI sequences. The challenges mentioned in the introduction (insufficient and repetitive texture, non-rigid motion of the plants, lighting changes, and jumpy motion) cause the rapid loss of the feature tracks. As a consequence, among others, of the small length of the feature tracks, the drift grows quickly and failures are most likely.

Figure 5 shows a cumulative histogram of the length of features tracked by S-PTAM in two representative sequences, 06 from the Rosario dataset and 03 from KITTI. Note the higher amount of small-length tracks in

rotation quaternion and a 3D translation vector. Since the rear_wheel_odometry and the base_link coordinate systems are coincident, we publish the odometry messages on the base_link system and remove the rear_wheel_odometry frame from the **tf** message for clarity.

4.6. Wheel odometry

We generated the robot wheel odometry using the Ackerman model (Weinstein and Moore, 2010). The wheelbase of our robot is 1.6 m, the steering angle $\delta \in [-19, 19]$ degrees, and the wheel diameter 0.57 m. Note that the dataset includes the post-processed odometry and the raw one, directly read from the sensors, in case another kinematic model is preferred.

4.7. Ground truth

We provide a positional GPS-RTK ground truth in order to assess the visual odometry (VO) and SLAM accuracies. Since the IMU does not have a magnetometer, no global orientation is provided.
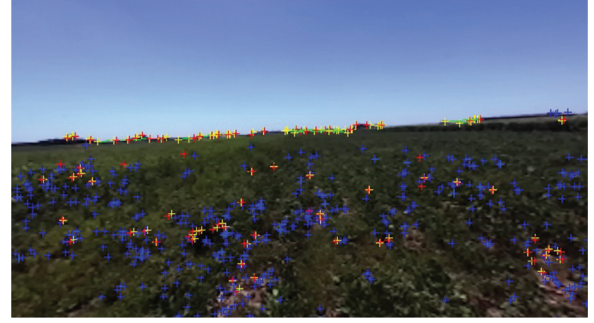
the Rosario sequence, illustrating the challenges in having high-quality and long feature tracks in agricultural scenes.

Finally, Figure 6 shows a representative frame of our dataset where we can see the tracked features. Note, first, in blue, the high number of map points that cannot be matched in this particular frame. Observe also that the number of features tracked (matches in red, map point projections in yellow) is moderate. As mentioned, this small number of tracks and its small duration causes drift.

6. Development tools

In order to access the robot sensors and collect the raw data, we developed several tools that capture the frames from the ZED stereo camera and the data from the IMU, the GPS-RTK, and the motor encoders. In the camera recording software we decoupled the image recording and writing processes, to avoid losing frames. We implemented an application using a producer–consumer multi-thread architecture. This is, one thread is in charge of reading the images captured by the camera and pushing them in a first in first out (FIFO) queue. A second thread pulls the images from the queue, in the order they were stored, and saves them on the disk.

We developed a set of Python scripts to generate the ROS messages from the raw data and to parse the calibration parameters from one format to another. We summarize here two of the script most relevant for the processing of the data.

- *create_bagfile.py* generates a rosbag from the raw data recorded by all of our sensors. It also considers the intrinsic and extrinsic calibration parameters to generate the CameraInfo messages for each camera.
- *imu_convertion.py* processes the IMU data in order to have the acceleration expressed in meters per second squared and the angular velocity in radians per second. This script also removes the offsets estimated by the Kalibr tool calibration.

We used the *Allan Tools* software[6] to obtain the IMU noise model through the *Allan variance*.

All the tools described are provided, along with the dataset. The aim is to allow and facilitate the manipulation of the raw data to replicate our results, to obtain new ones, and to help in the recording of new datasets with the sensors we used.

7. Conclusions and future work

The aim of this work was the public release of a dataset, as a tool for other researchers to evaluate and improve their algorithms. We targeted the SLAM and odometry communities working with visual sensors (the dataset contains calibrated stereo data) and with fusion of odometric, inertial, and visual information.

The sequences were recorded in large agricultural environments, a non-traditional scenario for localization and mapping where few datasets exist. The monotony of the surroundings of a robot and the lack of texture are challenges for its visual positioning, that are present in our dataset. We believe that our dataset will contribute to the development of methodologies and algorithms suitable for such an important area of work as agriculture.

ORCID iD

Taihú Pire   https://orcid.org/0000-0001-5621-6474

Notes

1 See https://www.stereolabs.com/zed/
2 See https://emlid.com/reach/
3 See https://www.e-consystems.com/
4 See http://www.intel.com
5 See http://wiki.ros.org/ar_track_alvar
6 See https://github.com/GAVLab/allan_variance

References

Alencastre-Miranda M, Davidson JR, Johnson RM, Waguespack H and Krebs HI (2018) Robotics for sugarcane cultivation: Analysis of billet quality using computer vision. *IEEE Robotics and Automation Letters* 3(4): 3828–3835.

Allan DW (1966) Statistics of atomic frequency standards. *Proceedings of the IEEE* 54(2): 221–230.

Blanco-Claraco JL, Moreno-Dueñas FÁ and González-Jiménez J (2014) The Málaga urban dataset: High-rate stereo and LIDAR in a realistic urban scenario. *The International Journal of Robotics Research* 33(2): 207–214.

Burri M, Nikolic J, Gohl P, et al. (2016) The EuRoC micro aerial vehicle datasets. *The International Journal of Robotics Research* 35(10): 1157–1163.

Carlevaris-Bianco N, Ushani AK and Eustice RM (2016) University of Michigan North Campus long-term vision and LIDAR dataset. *The International Journal of Robotics Research* 35(9): 1023–1035.

Chebrolu N, Lottes P, Schaefer A, Winterhalter W, Burgard W and Stachniss C (2017) Agricultural robot dataset for plant classification, localization and mapping on sugar beet fields. *The International Journal of Robotics Research* 36(10): 1045–1052.

Di Cicco M, Potena C, Grisetti G and Pretto A (2017) Automatic model based dataset generation for fast and accurate crop and weeds detection. In: *Proceedings of the IEEE/RSJ International Conference on Intelligent Robots and Systems (IROS)*.

Dias PA, Tabb A and Medeiros H (2018) Multispecies fruit flower detection using a refined semantic segmentation network. *IEEE Robotics and Automation Letters* 3(4): 3003–3010.

Fentanes JP, Gould I, Duckett T, Pearson S and Cielniak G (2018) 3D soil compaction mapping through kriging-based exploration with a mobile robot. *arXiv preprint arXiv:1803.08069*.

Furgale P, Barfoot TD and Sibley G (2012a) Continuous-time batch estimation using temporal basis functions. In: *Proceedings of the IEEE International Conference on Robotics and Automation (ICRA)*. IEEE, pp. 2088–2095.

Furgale P, Carle P, Enright J and Barfoot TD (2012b) The Devon Island rover navigation dataset. *The International Journal of Robotics Research* 31(6): 707–713.

Furgale P, Rehder J and Siegwart R (2013) Unified temporal and spatial calibration for multi-sensor systems. In: *Proceedings of the 2013 IEEE/RSJ International Conference on Intelligent Robots and Systems (IROS)*. IEEE, pp. 1280–1286.

Geiger A, Lenz P, Stiller C and Urtasun R (2013) Vision meets robotics: The KITTI dataset. *The International Journal of Robotics Research* 32(11): 1231–1237.

Griffith S, Chahine G and Pradalier C (2017) Symphony Lake dataset. *The International Journal of Robotics Research* 36(11): 1151–1158.

Haug S and Ostermann J (2014) A crop/weed field image dataset for the evaluation of computer vision based precision agriculture tasks. In: *Proceedings of the European Conference on Computer Vision (ECCV)*. Berlin: Springer, pp. 105–116.

Leung K, Lühr D, Houshiar H, et al. (2017) Chilean underground mine dataset. *The International Journal of Robotics Research* 36(1): 16–23.

Maddern W, Pascoe G, Linegar C and Newman P (2017) 1 year, 1000 km: The Oxford RobotCar dataset. *The International Journal of Robotics Research* 36(1): 3–15.

Majdik AL, Till C and Scaramuzza D (2017) The Zurich urban micro aerial vehicle dataset. *The International Journal of Robotics Research* 36(3): 269–273.

Maye J, Furgale P and Siegwart R (2013) Self-supervised calibration for robotic systems. In: *Proceedings of the 2013 IEEE Intelligent Vehicles Symposium (IV)*. IEEE, pp. 473–480.

Miller M, Chung SJ and Hutchinson S (2018) The visual–inertial canoe dataset. *The International Journal of Robotics Research* 37(1): 13–20.

Mur-Artal R and Tardós JD (2017) ORB-SLAM2: An open-source SLAM system for monocular, stereo, and RGB-D cameras. *IEEE Transactions on Robotics* 33(5): 1255–1262.

Olson E (2011) AprilTag: A robust and flexible visual fiducial system. In: *Proceedings of the 2011 IEEE International Conference on Robotics and Automation (ICRA)*. IEEE, pp. 3400–3407.

Pandey G, McBride JR and Eustice RM (2011) Ford Campus vision and LIDAR data set. *International Journal of Robotics Research* 30(13): 1543–1552.

Pezzementi Z, Tabor T, Hu P, et al. (2018) Comparing apples and oranges: Off-road pedestrian detection on the national robotics engineering center agricultural person-detection dataset. *Journal of Field Robotics* 35(4): 545–563.

Pire T, Fischer T, Castro G, De Cristóforis P, Civera J and Jacobo Berlles J (2017) S-PTAM: Stereo parallel tracking and mapping. *Robotics and Autonomous Systems* 93: 27–42.

Pire T, Fischer T, Civera J, De Cristóforis P and Berlles JJ (2015) Stereo parallel tracking and mapping for robot localization. In: *Proceedings of the IEEE/RSJ International Conference on Intelligent Robots and Systems (IROS)*, pp. 1373–1378.

Pistarelli M, Pire T and Kofman E (2017) Caracterización de un sistema GPS RTK de bajo costo. In: *Actas de las IX Jornadas Argentinas de Robótica*. Córdoba, Argentina: Facultad Regional Córdoba de la Universidad Tecnológica Nacional, pp. 11–16.

Ruiz-Sarmiento J, Galindo C and González-Jiménez J (2017) Robot@home, a robotic dataset for semantic mapping of home environments. *The International Journal of Robotics Research* 36(2): 131–141.

Sa I, Chen Z, Popović M, et al. (2018) weedNet: Dense semantic weed classification using multispectral images and MAV for smart farming. *IEEE Robotics and Automation Letters* 3(1): 588–595.

Smith M, Baldwin I, Churchill W, Paul R and Newman P (2009) The New College vision and laser data set. *The International Journal of Robotics Research* 28(5): 595–599.

Sturm J, Engelhard N, Endres F, Burgard W and Cremers D (2012) A benchmark for the evaluation of RGB-D SLAM systems. In: *Proceedings of the 2012 IEEE/RSJ International Conference on Intelligent Robots and Systems (IROS)*. IEEE, pp. 573–580.

Tong CH, Gingras D, Larose K, Barfoot TD and DupuisÉ (2013) The Canadian planetary emulation terrain 3D mapping dataset. *The International Journal of Robotics Research* 32(4): 389–395.

Weinstein AJ and Moore KL (2010) Pose estimation of Ackerman steering vehicles for outdoors autonomous navigation. In: *Proceedings of the 2010 IEEE International Conference on Industrial Technology*, pp. 579–584.